

RV-GAN : Retinal Vessel Segmentation from Fundus Images using Multi-scale Generative Adversarial Networks

Sharif Amit Kamran,
University of Nevada, Reno
skamran@nevada.unr.edu

Stewart Lee Zuckerbrod
Houston Eye Associates
szuckerbrod@houstoneye.com

Khondker Fariha Hossain
Deakin University
khossain@deakin.edu.au

Kenton M. Sanders
University of Nevada, Reno
ksanders@med.unr.edu

Alireza Tavakkoli
University of Nevada, Reno
tavakkol@unr.edu

Salah A. Baker
University of Nevada, Reno
sabubaker@med.unr.edu

Abstract

Retinal vessel segmentation contributes significantly to the domain of retinal image analysis for the diagnosis of vision-threatening diseases. With existing techniques the generated segmentation result deteriorates when thresholded with higher confidence value. To alleviate from this, we propose RVGAN, a new multi-scale generative architecture for accurate retinal vessel segmentation. Our architecture uses two generators and two multi-scale autoencoder based discriminators, for better microvessel localization and segmentation. By combining reconstruction and weighted feature matching loss, our adversarial training scheme generates highly accurate pixel-wise segmentation of retinal vessels with threshold ≥ 0.5 . The architecture achieves AUC of 0.9887, 0.9814, and 0.9887 on three publicly available datasets, namely DRIVE, CHASE-DB1, and STARE, respectively. Additionally, RV-GAN outperforms other architectures in two additional relevant metrics, Mean-IOU and SSIM.

1. Introduction

The fundoscopic exam is a procedure to diagnose different retinal degenerative diseases such as Diabetic Retinopathy, Macular Edema, Cytomegalovirus Retinitis, etc. This examination provides necessary information that can be utilized by Ophthalmologists to detect symptoms for vision-threatening diseases [36]. To diagnosis these vascular diseases, an automated retinal vessel segmentation system is required that can find abnormalities in blood vessels of the retinal subspace. In addition to that, this system can be utilized for extracting complex morphological attributes, performing temporal or multimodal image registration [42], retinal image mosaic synthesis, optic disk identification,

and fovea localization [23]. So far, many image processing and machine learning-based approaches have been proposed for retinal vessel segmentation [35, 11, 32, 20]. However, such methods fail to precisely pixel-wise segment blood vessels, due to bad illumination, periodic noises, etc. This becomes more problematic when extracting microvessels with the optic-disc present in the background. Moreover, attributes like retinal boundary, bright and dark lesions present in the subspace can create false-positive segmentation [11].

In recent times, UNet based deep learning architectures have become very popular for retinal vessel segmentation. UNet consists of an encoder to capture context information and a decoder for enabling precise localization[33]. Many derivative works based on UNet have been proposed, such as Dense-UNet, Deformable UNet[15], IterNet [24] etc. These models were able to achieve remarkable results for vessel segmentation. Especially, IterNet achieving state-of-the-art results and precisely detecting microvessel in the retinal subspace. But with the current deep learning architectures, the generated segmentation map deteriorates if the prediction values are thresholded to a higher confidence score. This is clearly illustrated in Fig. 1, where the threshold value is set to $t = 0.5$ and for three different data-set, we see that the UNet derived architectures performing poorly. To alleviate this, we need an architecture that can differentiate and discard irrelevant global and local information in the retinal subspace. Additionally, discriminative features need to be extracted and utilized for prediction with a high confidence score. By taking all of these into account, we propose Retinal-Vessel GAN or **RV-GAN**, consisting of coarse and fine generators and multi-scale autoencoder-based discriminators for producing highly accurate segmentation of blood vessel with strong confidence scores. Additionally, we utilize a new weighted feature matching loss with inner and outer weights and combine it with reconstruction and hinge

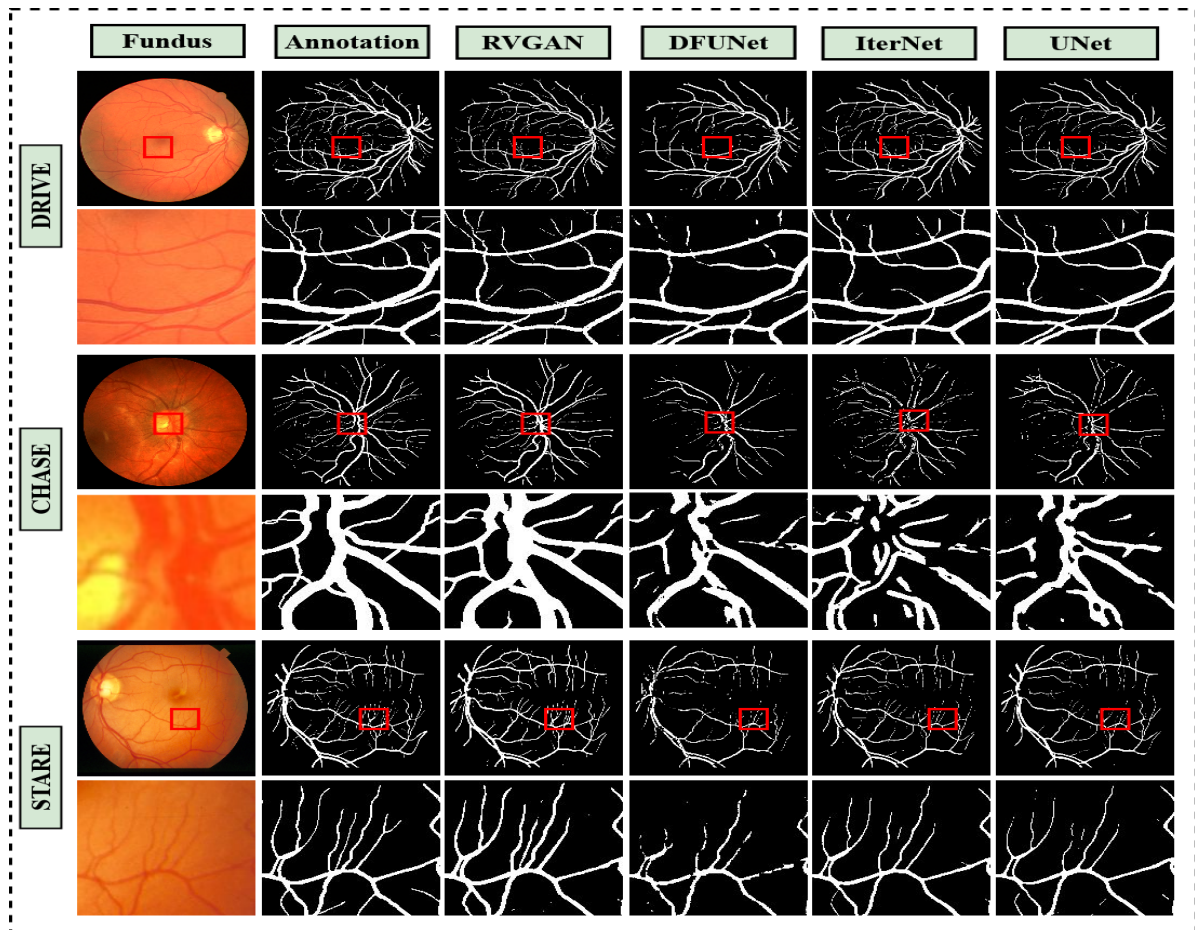


Figure 1: RV-GAN segments vessel with better precision than other architectures. The 1st row is the whole image, while 2nd row is specific zoomed-in area of the image. The Red bounded box signifies the zoomed-in region. The figure illustrates retinal vessel segmentation with threshold, $t = 0.5$. RV-GAN generates better segmentation map with high confidence scores. The row contains DRIVE, CHASE-DB1 and STARE data-set. Whereas the column contains fundus images, human-annotations and segmentation maps for RV-GAN, DFUNet, IterNet and UNet.

loss for adversarial training of our architecture. From Fig. 1, it is apparent that our architecture produces segmentation map with high confidence score.

2. Literature Review

For a long time, Fully Convolutional Network (FCN) and its derivative architectures have been the state-of-the-art model for any image segmentation task. FCN is trained end-to-end for pixel-wise segmentation and spatially dense prediction tasks [28, 18]. The concept is to extract the raw image into a feature vector and transform it into a segmented image. On the other hand, UNet [33], an encoder-decoder architecture with skip connections, also utilizes this trait of extracting features from the images. The combination of FCN and UNet has been adopted for many retinal vessel segmentation tasks, such as IterNet [24], DUNet [15],

R2UNet [1] etc.

In recent times Generative Architectures have become popular for retinal image synthesis [16, 17], denoising [3, 8], and retinal vessel segmentation [36, 41]. While most architectures ensure high-quality image generation and image-to-image translation, they all rely on Patch-GAN [14] as a discriminator. The discriminator uses image patches to find discriminative features and dictate if the image is real or synthesized. Despite using auto-encoders in generators, pixel-wise segmentation result underperforms when coupled with Patch-GAN-based discriminators. The performance of such GAN architectures [36, 30, 41], even fails to exceed some of the single auto-encoder-based UNet architectures [15, 24]. Another important factor is, the confidence score is not taken into account while generating segmentation maps. As the outputs activation function can be sigmoid $[0 - 1]$ or TanH $[-1, 1]$ depending on the archi-

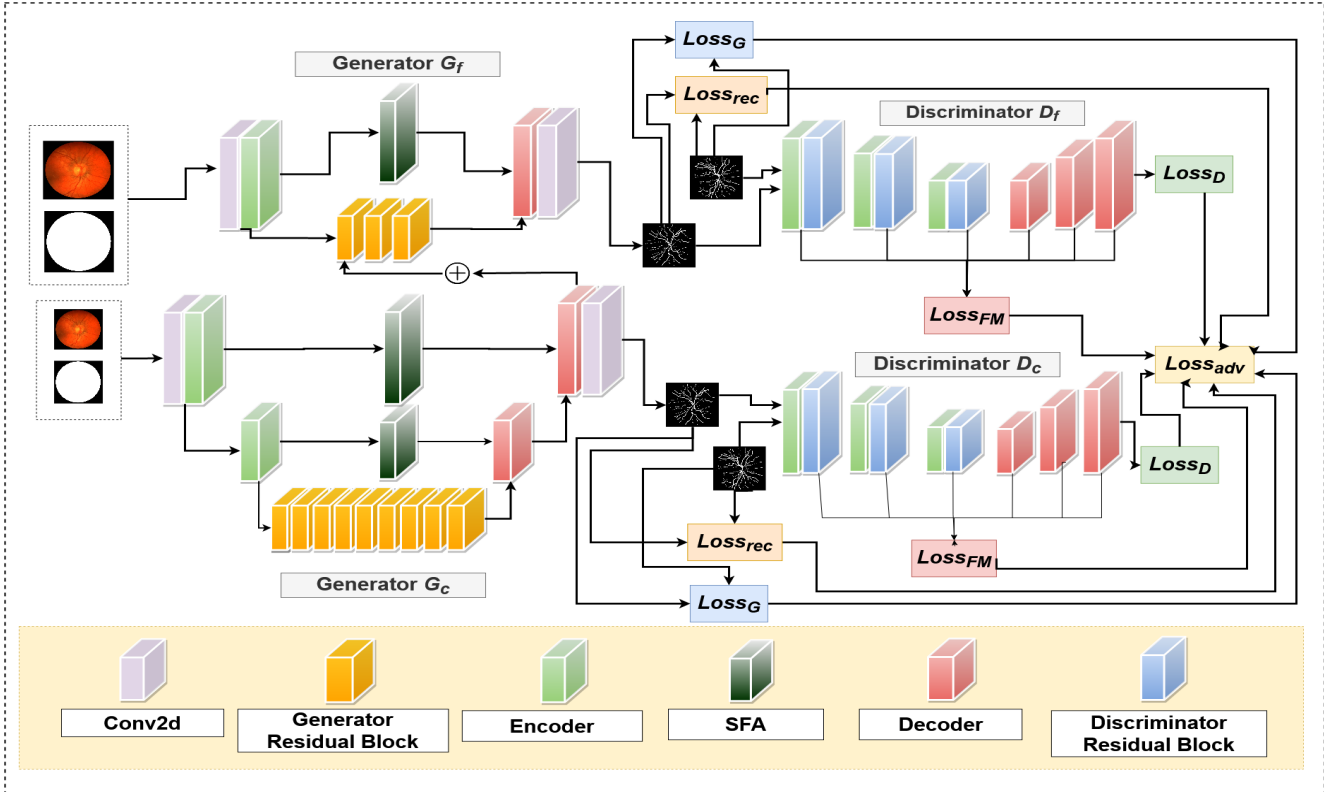


Figure 2: RV-GAN consisting of Coarse and Fine generators G_f, G_c and discriminators D_f, D_c . The generators incorporate reconstruction loss, $Loss_{rec}$ and Hinge loss $Loss_G$. Whereas the discriminators use weighted feature matching loss, $Loss_{fm}$ and Hinge loss $Loss_D$. All of these losses are multiplied by weight multiplier and then added in the final adversarial loss, $Loss_{adv}$. The generators consist of Encoder, Decoder, SFA and its distinct residual blocks. On the other hand, the discriminators consist of Encoder, Decoder and counterpart residual blocks.

texture, the resulting pixel value in grayscale can range between $[0 - 255]$. The same predicted segmentation map with low confidence might look highly accurate with a threshold value between $0.1 - 0.2$ (the range is between $[0 - 1]$). Whereas the segmentation starts to deteriorate when the threshold is increased to $0.5 - 0.7$. To address all of the aforementioned challenges, an architecture is needed that can generate an accurate segmentation map with high confidence scores. We propose a new multi-scale generative adversarial network, with the following improvements: *i*) We employ coarse and fine generators with spatial aggregation block and multi-scale autoencoders as a discriminator to extract better discriminative features and synthesize accurate segmentation maps, *ii*) We incorporate a weighted feature matching loss for discriminators along with a reconstruction loss for generators. The adversarial loss combines all the above along with hinge loss for training the GAN in an end-to-end manner. *iii*) Lastly, we benchmark our architecture on two new relevant metrics for evaluating accurate segmentation map and structural similarity, namely MeanIOU and SSIM.

3. Proposed Methodology

In the next section, we give a detailed outline of our multi-scale generators in subsection 3.1. Next, we elaborate our Encoder-Decoder, Identity Residual Block and SFA block in subsection 3.2, 3.3, 3.4. After that, we delve into the auto-encoder based discriminators and their connectivity with the multi-scale generators to outline the end-to-end system for the generative network in subsections 3.5. Conclusively, in subsection 3.6, we explain the associated losses with each of the architectures and weight distributions of these losses that form the proposed GAN model.

3.1. Multi-scale Generators

Pairing multi-scale coarse and fine generators produces high-quality domain-specific retinal image synthesis, as observed in recent generative networks, such as Fundus2Angio [17], Attention2Angio [16] and V-GAN [37] etc. Inspired by this, we also adopt this feature in our architecture by using two generators (G_{fine} and G_{coarse}), as visualized in Fig. 2. The generator G_{fine} synthesizes fine-

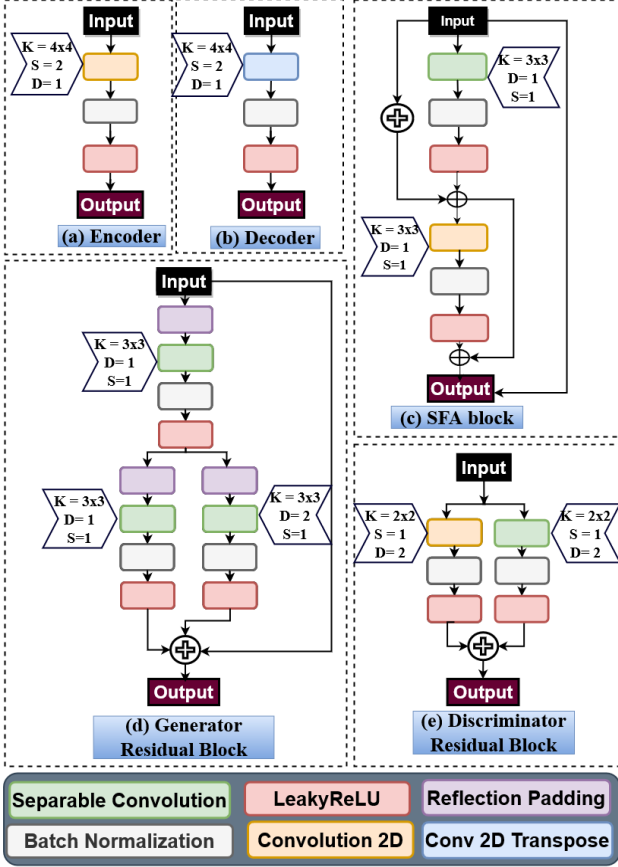


Figure 3: Proposed Encoder, Decoder, Spatial Feature Aggregation block, Generator and Discriminator Residual blocks. Here, $K = \text{Kernel size}$, $S = \text{Stride}$, $D = \text{Dilation Rate}$.

grained vessel segmentation images by extracting local features such as micro branches, connections, blockages, etc. In contrast, the generator G_{coarse} tries to learn and conserve global information, such as the structures of the macro branches, while producing less detailed microvessel segmentation. The generators consist of multiple encoders, decoder, spatial-aggregation blocks, residual identity blocks, and a feature appending block between the fine and coarse generators. The input and output dimension of G_{fine} is 128×128 . Similarly, G_{coarse} takes an image with half the size of G_{fine} (64×64) and generates a segmentation map of the same size as input. Additionally, the G_{coarse} outputs a feature vector of the size $64 \times 64 \times 64$, which is element-wise summed with one of the intermediate layers of G_{fine} using the feature appending operation. Both G_{coarse} and G_{fine} takes real fundus image and a mask for the fovea as input. The detailed structure of these generators is illustrated in Fig. 2. In the concurrent sections, we elaborate on each of these atomic blocks in depth.

3.2. Residual Encoder and Decoder Blocks

As both our generators and discriminators are auto-encoders, they consist of both encoder blocks for downsampling the feature maps. On the contrary, only the generators use decoder blocks for upsampling to get the desired feature maps and output. The encoder block comprises of a convolution layer, a batch-norm layer [13] and a Leaky-ReLU activation function consecutively and is illustrated in Fig. 3(a). Contrarily, the decoder block consists of a transposed convolution layer, batch-norm [13], and Leaky-ReLU activation layer successively and can be visualized in Fig.3(b). We use the encoder twice for $2 \times$ downsampling in G_{coarse} . This is followed by nine successive residual identity blocks. Finally, the decoder blocks are used to upsample $2 \times$ again to make the spatial dimension the same as the input. For G_{fine} , we utilize the encoder once, and after placing three residual identity blocks, a single decoder is employed to get the same spatial dimension as the input. Kernel size, $k = 4$, and stride, $s = 2$ is applied for both of our convolutions and transposed convolution layers.

3.3. Distinct Identity Blocks for Generator & Discriminator

For spatial and depth feature propagation, residual identity blocks have become go-to building blocks for image style transfer, image inpainting, and image segmentation tasks [34, 39, 5, 4, 31]. The original design consisted of a residual block with two consecutive convolution layers and a skip connection that adds feature tensor of the input with the output. Vanilla convolution layers are both computationally inefficient and fail to retain accurate spatial and depth information, as opposed to separable convolution [6]. Separable convolution comprises of a depth-wise convolution and a point-wise convolution successively. As a result, it extracts and preserves depth and spatial features while forward propagating the network. Recent advancement in retinal image classification has shown that combining separable convolutional layers with dilation allows for more robust feature extraction [19]. We design two unique residual identity blocks, for our generators and discriminators, as illustrated in Fig. 3(d) & Fig. 3(e). The identity block for our generator consists of Reflection padding, Separable Convolution, Batch-Norm, and Leaky-ReLU layers followed by two branches of the same repetition of layers. In contrast, one branch consists of a separable convolution with a dilation rate of, $d = 1$ and the other with a dilation rate, $d = 2$. All the separable convolution layers have, kernel size, $k = 3$ and stride, $s = 1$. The skip connection and output of the two branches are all added together to produce the final output. In contrast, the residual block for the discriminator consists of two branches, one with a convolution layer, followed by Batch-Normalization and Leaky-ReLU activation function. The other one with the Separable convolution layer,

followed by Batch-Norm and Leaky-ReLU layers. Both the convolution and separable convolution have a kernel size of $k = 2$, dilation rate of $d = 2$ and stride, $s = 1$.

3.4. Spatial Feature Aggregation

In this section, we discuss our proposed spatial feature aggregation (SFA) block, as illustrated in Fig. 3(c). The block consists of two residual units. One with Searable Convolution, Batch-Norm, and Leaky-ReLU layer and one with Convolution, BatchNorm, and Leaky-ReLU layers. Both the separable convolution and convolution layer have kernel, $k = 3$, dilation rate, $d = 1$ and stride, $s = 1$. Additionally, there are three skip connections, one going from the input and being element-wise summed to the output of the first residual unit. The next one is coming from the input and being added with the output of the last residual unit. Lastly, the third one is coming out of the output of the first residual unit and being element-wise summed with the output of the last residual unit. We use spatial feature aggregation block for combining spatial and depth features from the bottom layers of the network with the top layers of the network, as illustrated in Fig. 2. G_{coarse} comprises of two SFA blocks, that connects each of the two encoders with the two decoders successively. Perversely, the G_{fine} has only one SFA block between the sole encoder and decoder. The rationale behind employing the SFA block is to extract and retain spatial and depth information, that is otherwise lost in deep networks. Consequently, these features can be combined with the learned features of the deeper layers of the network to get an accurate approximation, as observed in similar GAN architectures [43, 2].

3.5. Auto-encoder as Discriminators

For better pixel-wise segmentation, we need an architecture that can extract both global and local features from the image. To mitigate this underlying problem, we need a deep and dense architecture with lots of computable parameters. It, in turn, might lead to overfitting or vanishing gradient while training the model. To address this issue, rather than having a single dense segmentation architecture, we adopt light-weight discriminators as autoencoders, as proposed in Energy-based GANs [44]. Additionally, we use multi-scale discriminators for both our coarse and fine generators, as previously proposed in [22, 39]. The arrangement consists of two discriminators with variable sized input and can help with the overall adversarial training. We define two discriminators as D_f and D_c as illustrated in Fig. 2. We resize each of the coarse and fine mask and fundus with size 128×128 and 64×64 by a factor of 2 using the Lanczos filter [9]. D_f and D_c have identical blocks consisting of three repetitive encoder and residual block pairs (in Fig. 3(a) and Fig. 3(e)). This is followed by three decoders as illustrated in Fig. 3(b). Ultimately, a convolution layer is used for getting spatial di-

mension of 128×128 for D_f and 64×64 for D_c as outputs. By doing adversarial training, the discriminators try to distinguish real and synthesize retinal vessel segmentation output. D_c learns feature at a lower resolution and convinces the coarse generator, G_c , to retain more global features such as the macro branches and connections. Contrarily, the D_f dictates the fine generator, G_f , to produce more detailed local features such as microvessels and arteries. By doing this we combine features from both G_f and G_c while training them autonomously with their paired multi-scale auto-encoder based discriminators.

3.6. Weighted Objective and Adversarial Loss

With the given multi-scale discriminators, D_f, D_c , and generators, (G_f, G_c) , the objective function can be formed as Eq. 1. It’s a multi-objective problem of maximizing the loss of the discriminators while minimizing the loss of the generators.

$$\min_{G_f, G_c} \max_{D_f, D_c} \mathcal{L}_{adv}(G_f, G_c, D_f, D_c) \quad (1)$$

For adversarial training, we use Hinge-Loss [43, 26] as given in Eq. 2 and Eq. 3. Conclusively, all the fundus images and their corresponding segmentation map pairs are normalized, to $[-1, 1]$. As a result, it broadens the difference between the pixel intensities of the real and synthesized segmentation maps. In Eq. 4, we multiply $\mathcal{L}_{adv}(G)$ with λ_{adv} as weight multiplier. Next, we add $\mathcal{L}_{adv}(D)$ with the output of the multiplication.

$$\mathcal{L}_{adv}(D) = -\mathbb{E}_{x,y} [\min(0, -1 + D(x, y))] - \mathbb{E}_x [\min(0, -1 - D(x, G(x)))] \quad (2)$$

$$\mathcal{L}_{adv}(G) = -\mathbb{E}_{x,y} [(D(G(x), y))] \quad (3)$$

$$\mathcal{L}_{adv}(G, D) = \mathcal{L}_{adv}(D) + \lambda_{adv}(\mathcal{L}_{adv}(G)) \quad (4)$$

In Eq. 2 and Eq. 3, we first train the discriminators on the real fundus, x and real segmentation map, y . After that, we train with the real fundus, x , and synthesized segmentation map, $G(x)$. We begin by batch-wise training the discriminators D_f , and D_c for a couple of iterations on the training data. Following that, we train the G_c while keeping the weights of the discriminators frozen. In a similar fashion, we train G_f on a batch training image while keeping weights of all the discriminators frozen.

The generators also incorporate the reconstruction loss (Mean Squared Error) as shown in Eq. 5. By utilizing the loss we ensure the synthesized images contain more realistic microvessel, arteries, and vascular structure. We also incorporate a weighted feature matching loss with all our discriminators and is given in Eq. 6.

$$\mathcal{L}_{rec}(G) = \mathbb{E}_{x,y} \|G(x) - y\|^2 \quad (5)$$

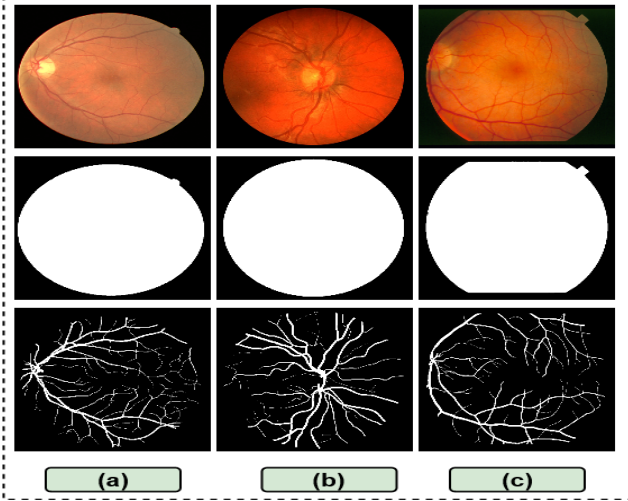


Figure 4: Raw images, masks and annotation from the dataset (a) DRIVE (b) CHASE-DB1 (c) STARE

$$\mathcal{L}_{fm}(G, D_n) = \mathbb{E}_{x,y} \sum_{i=1}^k \frac{\lambda_w^i}{N} \|D_n^i(x, y) - D_n^i(x, G(x))\| \quad (6)$$

For Eq. 5, \mathcal{L}_{rec} is the reconstruction loss for human-annotated segmentation map, y , given a generated segmentation map, $G(x)$. We use this loss for both G_f and G_c so that the model can generate highly accurate segmentation maps of different scales. Eq. 6 is calculated by taking the features from each of the output of the encoder and decoder blocks of the discriminator by first inserting the real and synthesize segmentation maps consecutively. Here, λ_w is the inner weight multiplier for each of the extracted feature maps. The weight values are between $[0, 1]$, and we use a higher weight value for the decoder feature maps than the encoder feature maps. By incorporating Eq. 4, 5 and 6, we can formulate our final objective function as given in Eq. 7.

$$\min_{G_f, G_c} \left(\max_{D_f, D_c} (\mathcal{L}_{adv}(G_f, G_c, D_f, D_c)) + \lambda_{rec} [\mathcal{L}_{rec}(G_f, G_c)] + \lambda_{fm} [\mathcal{L}_{fm}(G_f, G_c, D_f, D_c)] \right) \quad (7)$$

Here, λ_{adv} , λ_{rec} , and λ_{fm} implies different weights, that is multiplied with their respective losses. The loss weighting decides which architecture to prioritize while training. For our system, more weights are given to the $\mathcal{L}_{adv}(G)$, \mathcal{L}_{rec} , \mathcal{L}_{fm} , and thus we select bigger λ values for those.

4. Experiments

In the next section, we detail our model experiments and evaluate our architecture based on qualitative and quantitative metrics. First, we elaborate on the structuring and pre-processing of our dataset in Sec. 4.1. Then detail our

Algorithm 1 RV-GAN training

Input: $x_i \in X, m_i \in M, y_i \in Y$

Output: G_f, G_c

- 1: **Initialize hyper-parameters:**
 $max_epoch, b, max_d_iter, \omega_D^c, \omega_D^f, \omega_G^c, \omega_G^f, \alpha_D^c, \alpha_D^f, \alpha_G^c, \alpha_G^f, \beta_D^c, \beta_D^f, \beta_G^c, \beta_G^f, \lambda_{rec}, \lambda_{fm}, \lambda_w, \lambda_{adv}$
- 2: **for** $e = 0$ to max_epoch **do**
- 3: Sample $x_f, x_c, m_f, m_c, y_f, y_c$, using batch-size b
- 4: **for** $d_iter = 0$ to max_d_iter **do**
- 5: $\mathcal{L}_{adv}(D) \leftarrow D_c(x_c, y_c), D_f(x_f, y_f)$
- 6: $\mathcal{L}_{adv}(D) \leftarrow D_c(x_c, G_c(x_c, m_c)), D_f(x_f, G_f(x_f, m_f))$
- 7: $\mathcal{L}_{adv}(G) \leftarrow G_c(x_c, m_c), G_f(x_f, m_f)$
- 8: $\mathcal{L}_{adv}(G, D) \leftarrow \mathcal{L}_{adv}(D) + \lambda_{adv}(\mathcal{L}_{adv}(G))$
- 9: $\omega_D^c \leftarrow \omega_D^c + Adam(D_c, G_c, \omega_D^c, \alpha_D^c, \beta_D^c)$
- 10: $\omega_D^f \leftarrow \omega_D^f + Adam(D_f, G_f, \omega_D^f, \alpha_D^f, \beta_D^f)$
- 11: **end for**
- 12: **Freeze** ω_D^c, ω_D^f
- 13: Sample x_f, x_c, y_f, y_c , using batch-size b
- 14: $\mathcal{L}_{rec}(G_c) \leftarrow G(x_c, m_c), y_c$
- 15: $\mathcal{L}_{rec}(G_f) \leftarrow G(x_f, m_f), y_f$
- 16: $\omega_G^c \leftarrow \omega_G^c + Adam(G_c, \omega_G^c, \alpha_G^c, \beta_G^c)$
- 17: $\omega_G^f \leftarrow \omega_G^f + Adam(G_f, \omega_G^f, \alpha_G^f, \beta_G^f)$
- 18: **Unfreeze** ω_D^c, ω_D^f
- 19: $\mathcal{L}_{fm}(D_c, \lambda_w) \leftarrow D_c^n(x_c, y_c), D_f^n(x_c, G(x_c, m_c)), \lambda_w^n$
- 20: $\mathcal{L}_{fm}(D_f, \lambda_w) \leftarrow D_f^n(x_f, y_f), D_f^n(x_f, G(x_f, m_f)), \lambda_w^n$
- 21: $\omega_D^c \leftarrow \omega_D^c + Adam(D_c, G_c, \omega_D^c, \alpha_D^c, \beta_D^c)$
- 22: $\omega_D^f \leftarrow \omega_D^f + Adam(D_f, G_f, \omega_D^f, \alpha_D^f, \beta_D^f)$
- 23: **Freeze** ω_D^c, ω_D^f
- 24: $\mathcal{L}_{adv}(D) \leftarrow D_c(x_c, y_c), D_f(x_f, y_f)$
- 25: $\mathcal{L}_{adv}(D) \leftarrow D_c(x_c, G_c(x_c, m_c)), D_f(x_f, G_f(x_f, m_f))$
- 26: $\mathcal{L}_{adv}(G) \leftarrow G_c(x_c, m_c), G_f(x_f, m_f)$
- 27: $\mathcal{L}_{adv}(G, D) \leftarrow \mathcal{L}_{adv}(D) + \lambda_{adv}(\mathcal{L}_{adv}(G))$
- 28: $\omega_D^c \leftarrow \omega_D^c + Adam(D_c, G_c, \omega_D^c, \alpha_D^c, \beta_D^c)$
- 29: $\omega_D^f \leftarrow \omega_D^f + Adam(D_f, G_f, \omega_D^f, \alpha_D^f, \beta_D^f)$
- 30: Save weights and snapshot of G_f, G_c
- 31: $\mathcal{L} \leftarrow \mathcal{L}_{adv} + \lambda_{rec}(\mathcal{L}_{rec}) + \lambda_{fm}(\mathcal{L}_{fm})$
- 32: **end for**

hyper-parameter selection and tuning in Sec. 4.2. Next, we describe our adversarial training scheme in Sec. 4.3. Lastly, we compare our architecture with existing state-of-the-art generative models based on some quantitative evaluation metrics in Sec. 4.4.

4.1. Dataset

For benchmarking our model's performance, we use three retinal segmentation datasets, namely, DRIVE [38],

CHASE-DB1 [29], and STARE [12], as shown in the first row of Fig. 4. They are all in different formats and different image sizes. The images are respectively in *.tif* (565×584), *.jpg* (999×960), and *.ppm* (700×605) formats. We train three different RV-GAN networks with each of these datasets. We use overlapping image patches with stride of 32 and an image size of 128×128 for training our model. For inference, overlapping image patches of stride 3 were extracted and then averaged over all overlapping patches. In the first row Fig. 4, we can see retinal fundus images and in the second row, the field of view (FoV) masks of the retinal images are illustrated. DRIVE dataset comes with official masks for the test images. However, the other two datasets do provide such masks along with the fundus images. For fair evaluation, we also generate the FoV masks for CHASE-DB1 and STARE dataset as done by Li et al. [24] The mask can be generated by simple color thresholding the fundus images, because the pixels out of FoV are usually close to black. DRIVE dataset contains 20 images for training and 20 images for testing. In CHASE-DB1 and STARE, there are no official train/test splits. So we use the same protocol splitting the data as in [24]. For CHASE-DB1 we use 20 images for training and 8 images for testing. And for the STARE data-set, we use 16 images for training and 4 images testing.

4.2. Hyper-parameter Initialization

For adversarial training, we used hinge loss [43, 26]. We picked $\lambda_{adv} = 10$ (Eq. 4), $\lambda_{rec} = 10$ (Eq. 5) and $\lambda_w = 10$, $\lambda_{fm} = 10$ (Eq. 6). We used Adam optimizer [21], with learning rate $\alpha = 0.0002$, $\beta_1 = 0.5$ and $\beta_2 = 0.999$. We train with mini-batches with batch size, $b = 24$ for 100 epochs in three stages. It took between 24-48 hours to train our model on NVIDIA P100 GPU depending on which data-set the model was trained on. Because DRIVE and STARE have lower number of image patches compared to CHASE-DB1 dataset, it takes less amount to train.

4.3. Training Steps

In this section, we elaborate on our detailed algorithm provided in Algorithm 1. To train our RV-GAN, we start by initializing all the hyper-parameters. Next, we sample a batch of the real fundus, mask, and segmentation images, x, m, y . We train the real fundus and segmentation map pairs with D_f, D_c . After that, we use G_f, G_c to synthesize segmentation map and use the real fundus and synthesized segmentation map, $x, G(x, m)$ to train discriminators D_f, D_c . Following that, we calculate the adversarial loss, $\mathcal{L}_{adv}(D, G)$, and update the weights. We freeze the weights of the discriminators. Next, we train the generators and calculate the $\mathcal{L}_{rec}(G)$ losses and update both generator’s weights. Subsequently, we unfreeze both discriminators weights, calculate the feature matching loss $\mathcal{L}_{fm}(D)$

and update the discriminator weights. In the final stage, we freeze both discriminator’s weights and jointly fine-tune all the discriminator and generators. We calculate the total loss by adding and multiplying with their relative weights. For testing, we save the snapshot of the model and its weights.

4.4. Quantitative Bench-marking

We compared our architecture with some best performing ones, including UNet [15], DenseBlock-UNet [25], Deform-UNet [15] and IterNet [24] as illustrated in Fig. 1. We trained and evaluated the first three architectures using their publicly available source code by ourselves on the three datasets. For IterNet, the pre-trained weight was provided, so we used that to get the inference result. Receiver-operating-characteristics (ROC) curve, illustrated in Fig. 5, was generated using the same weights and with a stride of 3 and image patches size of 128×128 . We visualize ROC for DRIVE in Fig. 5(a), STARE in Fig. 5(b), and CHASE-DB1 in Fig. 5(c), where our produced ROC shows better overall performance over other architectures. Next, we do a comparative analysis with existing retinal vessel segmentation architectures, which includes both UNet and GAN based models, such as Residual UNet [1], Recurrent UNet [1], R2UNet [1], and SUD-GAN [41], M-GAN [30]. The prediction results for DRIVE are provided in Table. 1, CHASE-DB1 in Table. 2 and STARE in Table. 3. We report traditional metrics such as F1-score, Sensitivity, Specificity, Accuracy, and AUC-ROC. Additionally, we use two other metrics for predicting accurate segmentation and structural similarity of the retinal vessels, namely Mean-IOU (Jaccard Similarity Coefficient) and Structural Similarity Index[40]. We chose Mean-IOU because its the gold standard for measuring segmentation results for many Semantic Segmentation Challenges such as Pascal-VOC2012 [10], MS-COCO [27], Cityscapes [7]. Contrarily, SSIM is a standard metric for evaluating GANs for image-to-image translation tasks. As illustrated in all the tables, our model outperforms both UNet derived architectures and recent GAN based models in terms of AUC-ROC, Mean-IOU, and SSIM, the three main metrics for this task. In Table. 2 and Table. 3, M-GAN achieves better Specificity and Accuracy. However, higher Specificity means better background pixel segmentation (True Negative), which is less essential than having better retinal vessel segmentation (True Positive). We want both, better Sensitivity and AUC-ROC, which equates to having a higher confidence score with threshold, $t \geq 0.5$. In Fig. 5 we can see that our True positive Rate (TPR) is always better than other architectures for all three data-set. As source codes and pre-trained weights weren’t provided for some of the architectures, we couldn’t report SSIM and Mean-IOU for those in Table. 1, Table. 2, and Table. 3.

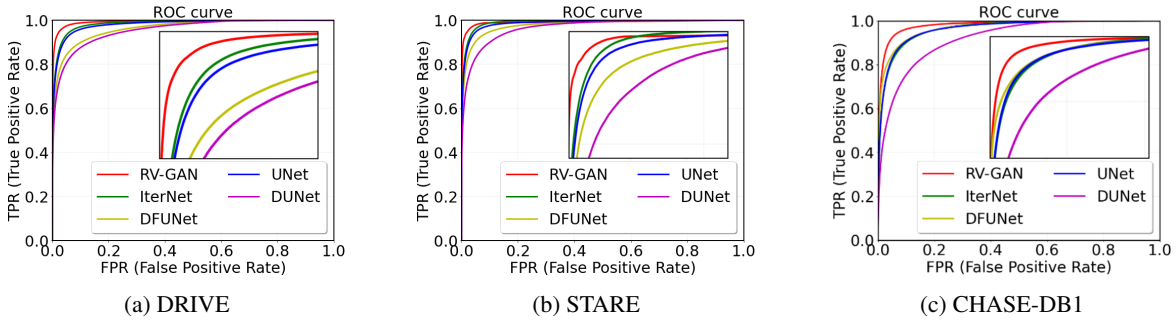


Figure 5: ROC Curves on (a) DRIVE (b) STARE (c) CHASE-DB1.

Table 1: Performance comparison on the DRIVE [38] dataset.

Method	Year	F1 Score	Sensitivity	Specificity	Accuracy	AUC-ROC	Mean-IOU	SSIM
UNet [15]	2018	0.8174	0.7822	0.9808	0.9555	0.9752	0.9635	0.8868
Residual UNet [1]	2018	0.8149	0.7726	0.9820	0.9553	0.9779	-	-
Recurrent UNet [1]	2018	0.8155	0.7751	0.9816	0.9556	0.9782	-	-
R2UNet [1]	2018	0.8171	0.7792	0.9813	0.9556	0.9784	-	-
DFUNet [15]	2019	0.8190	0.7863	0.9805	0.9558	0.9778	0.9605	0.8789
IterNet [24]	2019	0.8205	0.7735	0.9838	0.9573	0.9816	0.9692	0.9008
SUD-GAN [41]	2020	-	0.8340	0.9820	0.9560	0.9786	-	-
M-GAN [30]	2020	0.8324	0.8346	0.9836	0.9706	0.9868	-	-
RV-GAN (Ours)	2020	0.8690	0.7927	0.9969	0.9790	0.9887	0.9762	0.9237

Table 2: Performance comparison on the CHASE-DB1 [29] dataset.

Method	Year	F1 Score	Sensitivity	Specificity	Accuracy	AUC-ROC	Mean-IOU	SSIM
UNet [15]	2018	0.7993	0.7841	0.9823	0.9643	0.9812	0.9536	0.9029
DenseBlock-UNet [25]	2018	0.8006	0.8178	0.9775	0.9631	0.9826	0.9454	0.8867
DFUNet [15]	2019	0.8001	0.7859	0.9822	0.9644	0.9834	0.9609	0.9175
IterNet [24]	2019	0.8073	0.7970	0.9823	0.9655	0.9851	0.9584	0.9123
M-GAN [30]	2020	0.8110	0.8234	0.9938	0.9736	0.9859	-	-
RV-GAN (Ours)	2020	0.8957	0.8199	0.9806	0.9697	0.9914	0.9705	0.9266

Table 3: Performance comparison on the STARE [12] dataset.

Method	Year	F1 Score	Sensitivity	Specificity	Accuracy	AUC-ROC	Mean-IOU	SSIM
UNet [15]	2018	0.7595	0.6681	0.9915	0.9639	0.9710	0.9744	0.9271
DenseBlock-UNet [25]	2018	0.7691	0.6807	0.9916	0.9651	0.9755	0.9604	0.9034
DFUNet [15]	2019	0.7629	0.6810	0.9903	0.9639	0.9758	0.9701	0.9169
IterNet [24]	2019	0.8146	0.7715	0.9886	0.9701	0.9881	0.9752	0.9219
SUD-GAN [41]	2020	-	0.8334	0.9897	0.9663	0.9734	-	-
M-GAN [30]	2020	0.8370	0.8234	0.9938	0.9876	0.9873	-	-
RV-GAN (Ours)	2020	0.8323	0.8356	0.9864	0.9754	0.9887	0.9754	0.9292

5. Conclusion

In this paper, we proposed a new multi-scale generative architecture called RV-GAN. The architecture synthesizes precise venular structure segmentation with high confidence scores. Additionally, we illustrated its robust segmentation generation and retaining similarity with two new metrics. As a result, the proposed network can be efficiently employed to generate precise retinal blood vessel segmentation for various applications of ophthalmology. This is best

suited for finding analyzing retinal degenerative diseases and monitoring for future prognosis. We hope to extend this work for other areas of ophthalmological data modalities.

References

- [1] Md Zahangir Alom, Mahmudul Hasan, Chris Yakopcic, Tarek M Taha, and Vijayan K Asari. Recurrent residual convolutional neural network based on u-net (r2u-net) for medical image segmentation. *arXiv preprint arXiv:1802.06955*, 2018.

- [2] Xinyuan Chen, Chang Xu, Xiaokang Yang, and Dacheng Tao. Attention-gan for object transfiguration in wild images. In *Proceedings of the European Conference on Computer Vision (ECCV)*, pages 164–180, 2018.
- [3] Zailiang Chen, Ziyang Zeng, Hailan Shen, Xianxian Zheng, Peishan Dai, and Pingbo Ouyang. Dn-gan: Denoising generative adversarial networks for speckle noise reduction in optical coherence tomography images. *Biomedical Signal Processing and Control*, 55:101632, 2020.
- [4] Yunjey Choi, Minje Choi, Munyoung Kim, Jung-Woo Ha, Sunghun Kim, and Jaegul Choo. Stargan: Unified generative adversarial networks for multi-domain image-to-image translation. In *Proceedings of the IEEE conference on computer vision and pattern recognition*, pages 8789–8797, 2018.
- [5] Yunjey Choi, Youngjung Uh, Jaejun Yoo, and Jung-Woo Ha. Stargan v2: Diverse image synthesis for multiple domains. In *Proceedings of the IEEE/CVF Conference on Computer Vision and Pattern Recognition*, pages 8188–8197, 2020.
- [6] François Chollet. Xception: Deep learning with depthwise separable convolutions. In *Proceedings of the IEEE conference on computer vision and pattern recognition*, pages 1251–1258, 2017.
- [7] Marius Cordts, Mohamed Omran, Sebastian Ramos, Timo Rehfeld, Markus Enzweiler, Rodrigo Benenson, Uwe Franke, Stefan Roth, and Bernt Schiele. The cityscapes dataset for semantic urban scene understanding. In *Proceedings of the IEEE conference on computer vision and pattern recognition*, pages 3213–3223, 2016.
- [8] Zhao Dong, Guoyan Liu, Guangming Ni, Jason Jerwick, Lian Duan, and Chao Zhou. Optical coherence tomography image denoising using a generative adversarial network with speckle modulation. *Journal of Biophotonics*, 13(4):e201960135, 2020.
- [9] Claude E Duchon. Lanczos filtering in one and two dimensions. *Journal of applied meteorology*, 18(8):1016–1022, 1979.
- [10] Mark Everingham, SM Ali Eslami, Luc Van Gool, Christopher KI Williams, John Winn, and Andrew Zisserman. The pascal visual object classes challenge: A retrospective. *International journal of computer vision*, 111(1):98–136, 2015.
- [11] Muhammad Moazam Fraz, Paolo Remagnino, Andreas Hoppe, Bunyarit Uyyanonvara, Alicja R Rudnicka, Christopher G Owen, and Sarah A Barman. Blood vessel segmentation methodologies in retinal images—a survey. *Computer methods and programs in biomedicine*, 108(1):407–433, 2012.
- [12] AD Hoover, Valentina Kouznetsova, and Michael Goldbaum. Locating blood vessels in retinal images by piecewise threshold probing of a matched filter response. *IEEE Transactions on Medical Imaging*, 19(3):203–210, 2000.
- [13] Sergey Ioffe and Christian Szegedy. Batch normalization: Accelerating deep network training by reducing internal covariate shift. *arXiv preprint arXiv:1502.03167*, 2015.
- [14] Phillip Isola, Jun-Yan Zhu, Tinghui Zhou, and Alexei A Efros. Image-to-image translation with conditional adversarial networks. In *Proceedings of the IEEE conference on computer vision and pattern recognition*, pages 1125–1134, 2017.
- [15] Qiangguo Jin, Zhaopeng Meng, Tuan D Pham, Qi Chen, Leyi Wei, and Ran Su. Dunet: A deformable network for retinal vessel segmentation. *Knowledge-Based Systems*, 178:149–162, 2019.
- [16] Sharif Amit Kamran, Khondker Fariha Hossain, Alireza Tavakkoli, and Stewart Lee Zuckerbrod. Attention2angiogan: Synthesizing fluorescein angiography from retinal fundus images using generative adversarial networks. *arXiv preprint arXiv:2007.09191*, 2020.
- [17] Sharif Amit Kamran, Khondker Fariha Hossain, Alireza Tavakkoli, and Stewart Lee Zuckerbrod. Fundus2angio: A novel conditional gan architecture for generating fluorescein angiography images from retinal fundus photography. *arXiv preprint arXiv:2005.05267*, 2020.
- [18] S. A. Kamran and A. S. Sabbir. Efficient yet deep convolutional neural networks for semantic segmentation. In *2018 International Symposium on Advanced Intelligent Informatics (SAIN)*, pages 123–130, 2018.
- [19] S. A. Kamran, S. Saha, A. S. Sabbir, and A. Tavakkoli. Optic-net: A novel convolutional neural network for diagnosis of retinal diseases from optical tomography images. In *2019 18th IEEE International Conference On Machine Learning And Applications (ICMLA)*, pages 964–971, 2019.
- [20] Sharif Amit Kamran, Alireza Tavakkoli, and Stewart Lee Zuckerbrod. Improving robustness using joint attention network for detecting retinal degeneration from optical coherence tomography images. *arXiv preprint arXiv:2005.08094*, 2020.
- [21] Diederik P Kingma and Jimmy Ba. Adam: A method for stochastic optimization. *arXiv preprint arXiv:1412.6980*, 2014.
- [22] Chuan Li and Michael Wand. Precomputed real-time texture synthesis with markovian generative adversarial networks. In *European conference on computer vision*, pages 702–716. Springer, 2016.
- [23] Huiqi Li and Opas Chutatape. Automated feature extraction in color retinal images by a model based approach. *IEEE Transactions on biomedical engineering*, 51(2):246–254, 2004.
- [24] Liangzhi Li, Manisha Verma, Yuta Nakashima, Hajime Nagahara, and Ryo Kawasaki. Iternet: Retinal image segmentation utilizing structural redundancy in vessel networks. In *The IEEE Winter Conference on Applications of Computer Vision*, pages 3656–3665, 2020.
- [25] Xiaomeng Li, Hao Chen, Xiaojuan Qi, Qi Dou, Chi-Wing Fu, and Pheng-Ann Heng. H-denseunet: hybrid densely connected unet for liver and tumor segmentation from ct volumes. *IEEE transactions on medical imaging*, 37(12):2663–2674, 2018.
- [26] Jae Hyun Lim and Jong Chul Ye. Geometric gan. *arXiv preprint arXiv:1705.02894*, 2017.
- [27] Tsung-Yi Lin, Michael Maire, Serge Belongie, James Hays, Pietro Perona, Deva Ramanan, Piotr Dollár, and C Lawrence Zitnick. Microsoft coco: Common objects in context. In *European conference on computer vision*, pages 740–755. Springer, 2014.

- [28] Jonathan Long, Evan Shelhamer, and Trevor Darrell. Fully convolutional networks for semantic segmentation. In *Proceedings of the IEEE conference on computer vision and pattern recognition*, pages 3431–3440, 2015.
- [29] Christopher G Owen, Alicja R Rudnicka, Robert Mullen, Sarah A Barman, Dorothy Monokosso, Peter H Whincup, Jeffrey Ng, and Carl Paterson. Measuring retinal vessel tortuosity in 10-year-old children: validation of the computer-assisted image analysis of the retina (caiar) program. *Investigative ophthalmology & visual science*, 50(5):2004–2010, 2009.
- [30] Kyeong-Beom Park, Sung Ho Choi, and Jae Yeol Lee. Mgan: Retinal blood vessel segmentation by balancing losses through stacked deep fully convolutional networks. *IEEE Access*, 2020.
- [31] Taesung Park, Ming-Yu Liu, Ting-Chun Wang, and Jun-Yan Zhu. Semantic image synthesis with spatially-adaptive normalization. In *Proceedings of the IEEE Conference on Computer Vision and Pattern Recognition*, pages 2337–2346, 2019.
- [32] Elisa Ricci and Renzo Perfetti. Retinal blood vessel segmentation using line operators and support vector classification. *IEEE transactions on medical imaging*, 26(10):1357–1365, 2007.
- [33] Olaf Ronneberger, Philipp Fischer, and Thomas Brox. U-net: Convolutional networks for biomedical image segmentation. In *International Conference on Medical image computing and computer-assisted intervention*, pages 234–241. Springer, 2015.
- [34] Tamar Rott Shaham, Tali Dekel, and Tomer Michaeli. Singan: Learning a generative model from a single natural image. In *Proceedings of the IEEE International Conference on Computer Vision*, pages 4570–4580, 2019.
- [35] João VB Soares, Jorge JG Leandro, Roberto M Cesar, Herbert F Jelinek, and Michael J Cree. Retinal vessel segmentation using the 2-d gabor wavelet and supervised classification. *IEEE Transactions on medical imaging*, 25(9):1214–1222, 2006.
- [36] Jaemin Son, Sang Jun Park, and Kyu-Hwan Jung. Retinal vessel segmentation in fundoscopic images with generative adversarial networks. *arXiv preprint arXiv:1706.09318*, 2017.
- [37] Jaemin Son, Sang Jun Park, and Kyu-Hwan Jung. Towards accurate segmentation of retinal vessels and the optic disc in fundoscopic images with generative adversarial networks. *Journal of digital imaging*, 32(3):499–512, 2019.
- [38] Joes Staal, Michael D Abràmoff, Meindert Niemeijer, Max A Viergever, and Bram Van Ginneken. Ridge-based vessel segmentation in color images of the retina. *IEEE transactions on medical imaging*, 23(4):501–509, 2004.
- [39] Ting-Chun Wang, Ming-Yu Liu, Jun-Yan Zhu, Andrew Tao, Jan Kautz, and Bryan Catanzaro. High-resolution image synthesis and semantic manipulation with conditional gans. In *Proceedings of the IEEE conference on computer vision and pattern recognition*, pages 8798–8807, 2018.
- [40] Zhou Wang, Alan C Bovik, Hamid R Sheikh, and Eero P Simoncelli. Image quality assessment: from error visibility to structural similarity. *IEEE transactions on image processing*, 13(4):600–612, 2004.
- [41] Tiejun Yang, Tingting Wu, Lei Li, and Chunhua Zhu. Sudgan: Deep convolution generative adversarial network combined with short connection and dense block for retinal vessel segmentation. *Journal of Digital Imaging*, pages 1–12, 2020.
- [42] Frédéric Zana and Jean-Claude Klein. A multimodal registration algorithm of eye fundus images using vessels detection and hough transform. *IEEE transactions on Medical Imaging*, 18(5):419–428, 1999.
- [43] Han Zhang, Ian Goodfellow, Dimitris Metaxas, and Augustus Odena. Self-attention generative adversarial networks. In *International Conference on Machine Learning*, pages 7354–7363, 2019.
- [44] Junbo Zhao, Michael Mathieu, and Yann LeCun. Energy-based generative adversarial network. *arXiv preprint arXiv:1609.03126*, 2016.